


## Article

# Brain Network Modularity and Resilience Signaled by Betweenness Centrality Percolation Spiking

Parker Kotlarz <sup>1,2,\*</sup> , Marcelo Febo <sup>3</sup>, Juan C. Nino <sup>1</sup> and on behalf of the Alzheimer's Disease Neuroimaging Initiative <sup>†</sup>

<sup>1</sup> Department of Materials Science and Engineering, University of Florida, Gainesville, FL 32611, USA; jnino@mse.ufl.edu

<sup>2</sup> Harvard Medical School, Harvard University, Boston, MA 02115, USA

<sup>3</sup> Department of Psychiatry, University of Florida, Gainesville, FL 32611, USA; febo@ufl.edu

\* Correspondence: parkerkotlarz@hms.harvard.edu

<sup>†</sup> Data used in preparation of this article were obtained from the Alzheimer's Disease Neuroimaging Initiative (ADNI) database (adni.loni.usc.edu). As such, the investigators within the ADNI contributed to the design and implementation of ADNI and/or provided data but did not participate in analysis or writing of this report. A complete listing of ADNI investigators can be found at: [http://adni.loni.usc.edu/wp-content/uploads/how\\_to\\_apply/ADNI\\_Acknowledgement\\_List.pdf](http://adni.loni.usc.edu/wp-content/uploads/how_to_apply/ADNI_Acknowledgement_List.pdf).

**Abstract:** Modularity and resilience are fundamental properties of brain network organization and function. The interplay of these network characteristics is integral to understanding brain vulnerability, network efficiency, and neurocognitive disorders. One potential methodology to explore brain network modularity and resilience is through percolation theory, a sub-branch of graph theory that simulates lesions across brain networks. In this work, percolation theory is applied to connectivity matrices derived from functional MRI from human, mice, and null networks. Nodes, or regions, with the highest betweenness centrality, a graph theory quantifier that examines shortest paths, were sequentially removed from the network. This attack methodology led to a rapid fracturing of the network, resulting in two terminal modules connected by one transfer module. Additionally, preceding the rapid network fracturing, the average betweenness centrality of the network peaked in value, indicating a critical point in brain network functionality. Thus, this work introduces a methodological perspective to identify hubs within the brain based on critical points that can be used as an architectural framework for a neural network. By applying percolation theory to functional brain networks through a network phase-transition lens, network sub-modules are identified using local spikes in betweenness centrality as an indicator of brain criticality. This modularity phase transition provides supporting evidence of the brain functioning at a near-critical point while showcasing a formalism to understand the computational efficiency of the brain as a neural network.

**Keywords:** graph theory; percolation theory; connectomics; modularity; resilience; neural network



**Citation:** Kotlarz, P.; Febo, M.; Nino, J.C.; on behalf of the Alzheimer's Disease Neuroimaging Initiative. Brain Network Modularity and Resilience Signaled by Betweenness Centrality Percolation Spiking. *Appl. Sci.* **2024**, *14*, 4197. <https://doi.org/10.3390/app14104197>

Academic Editors: Alexander N. Pisarchik and Qi-Huang Zheng

Received: 12 March 2024

Revised: 13 April 2024

Accepted: 9 May 2024

Published: 15 May 2024



**Copyright:** © 2024 by the authors. Licensee MDPI, Basel, Switzerland. This article is an open access article distributed under the terms and conditions of the Creative Commons Attribution (CC BY) license (<https://creativecommons.org/licenses/by/4.0/>).

## 1. Introduction

The application of mathematical concepts of graph theory to networks derived from neuroimaging data continues to advance the understanding of the structural and functional properties of the human brain [1]. Graph theory quantifiers may serve as promising non-invasive biomarkers for investigating fundamental mechanisms of cognition, emotion, and neuropsychiatric and neurological diseases [2]. When applied to resting-state functional magnetic resonance imaging (rs-fMRI), a neuroimaging modality that measures brain activity by measuring changes in blood flow, graph theory algorithms may help reveal emergent properties of central nervous system function that would otherwise not be captured by seed-based fMRI analyses or single-circuit electrophysiological methods.

One such emergent topological feature is the grouping of nodes into communities or modules [3]. Modularity in rs-fMRI networks has been identified across many studies and

species, yet whether this is a principal feature of brain organization still warrants further investigation [4]. There are several approaches to investigating the modular organization of networks, and all are easily applied to brain networks. Modularity algorithms result in the identification of communities of non-overlapping nodes with high-density within-group edges and low-density between-module connections [3]. Additionally, recent work has incorporated machine learning models to identify brain network modules [5]. However, currently available methods are limited by the lack of information on the relationship between communities. Moreover, the development of quantifier markers for functional transitions between number, size, and connectivity between communities could help inform how modular organization is altered under disease conditions and the relationship between identified community nodes and network resilience.

The relationship between nodal communities can be understood using percolation theory, a sub-branch of graph theory that directly addresses network resilience through iterative and simulated destruction of network connectivity. Percolation can be broadly applied to structural and functional neuroimaging data from studies on brain development to neurological diseases such as Alzheimer's [6–15]. It is well established that percolation can identify distinct transition states, so-called phase transitions, which mark a critical point between a fully connected supercritical regime to subcritical disconnected configurations. In the present work, we harness percolation theory's ability to determine criticality to assess a novel marker of human brain function. In dynamic systems, such as neural networks, the boundary between order and chaos (i.e., edge of chaos) often contains states that allow maximized computational processing [16,17]. The ability to store, retrieve, and transfer information fluctuates between distinct states of network stability.

The interplay of percolation theory and network resilience has been extensively explored in theoretical and real-world networks [18,19]. In general, network resilience refers to the ability of a network to maintain functionality despite perturbations to the network [20]. Analytically, resilience can be defined as a differential equation that incorporates system dynamics, varying environmental conditions, and a state-dependent point [18]. This framework has been applied to human brain networks [21] to understand topological resilience in aging [22] and brain disorders [23].

However, the intersection of percolation theory, network resilience, and brain network modularity in examining network phase transitions and criticality has not been explored. By incorporating these aspects of network theory to study brain organization, computational network modules and properties can be extracted from real-world brain networks derived from neuroimaging. Our work, using connectomics derived from fMRI, yields significant supporting evidence of brain networks functioning at a near-critical point while also providing a new mechanism for identifying modules in the brain through betweenness centrality percolation. This work provides a framework for translating brain networks directly to neural networks for potential neuromorphic computing applications.

## 2. Materials and Methods

### 2.1. Mice Neuroimaging Methodology

The mouse data and image processing used in this study were originally collected and processed in Colon-Perez et al. [24], and previous connectomic analysis has been performed in our prior work [6]. Briefly, functional images of control littermates ( $n = 17$ , male = 9, female = 8) while under isoflurane anesthesia were collected using a single-shot spin-echo echo planar imaging (EPI) sequence with the following parameters: echo time (TE) = 15 ms, repetition time (TR) = 2 s, 180 repetitions,  $15 \times 11 \text{ mm}^2$  in plane, 14 slices with 0.9 mm thickness per slice, data matrix =  $64 \times 48$ . Mouse brain images were acquired on an 11.1 Tesla MRI scanner (MagneX Scientific Ltd., Oxford, UK) with a Resonance Research Inc. gradient set (RRI BFG-113/60, maximum gradient strength of 1500 mT/m at 150 Amps and a 130  $\mu\text{s}$  risetime; RRI, Billerica, MA, USA) and controlled by a Bruker Paravision 6.01 console (Bruker BioSpin, Billerica, MA, USA) as previously reported [25].

Average BOLD signals from each region of interest (ROI) were extracted based on their atlas location (90 ROIs, 45 per hemisphere) and used in voxel-wise cross-correlations to generate Pearson correlation maps and 4005 pairwise correlation coefficients to be imported to MATLAB as edge weights for network analysis. All correlation  $r$  values were  $z$ -transformed prior to statistical analyses. Correlation matrices were then normalized in MATLAB from zero to one. As a note, mouse results in this study are primarily used to demonstrate the generalizability of our methods across neuroimaging species.

## 2.2. Human Neuroimaging Methodology

### 2.2.1. Human Model Database and Image Acquisition

Data were obtained from the Alzheimer's Disease Neuroimaging Initiative (ADNI) repository ([ida.loni.usc.edu](http://ida.loni.usc.edu)). Data use received prior approval by the ADNI and the University of Florida Institutional Review Board (IRB201901878). Fifty-one control subjects were included in this study (female = 29, ages 70–93; male = 22, ages 71–95). For each subject, a T1-weighted magnetization-prepared rapid gradient echo (MPRAGE) scan and an echo planar image were originally collected on a 3 Tesla Siemens scanner. The MPRAGE had a  $240 \times 256 \times 176$  data matrix with  $1 \text{ mm}^3$  resolution, TE = 3 ms, TR = 2300 ms, inversion time (TI) = 900 ms, and a  $9^\circ$  flip angle. Resting-state EPI scans (eyes open) were collected with  $64 \times 64 \times 48$  slices at a  $3.4 \text{ mm}^3$  voxel resolution, and 197 volume repetitions with TE = 30 ms, TR = 3000 ms, and a  $90^\circ$  flip angle.

### 2.2.2. Human Model Image Preprocessing and Network Generation

Resting-state processing was carried out using software tools in Analysis of Functional NeuroImages (AFNI) [26], FMRIB Software Library (FSL) [27], and Advanced Normalization Tools (ANTs) [28]. A schematic of the image processing pipeline can be found in Figure 1. First, (1) the brain was extracted for both anatomical and functional scans using FSL BET, then (2) the scans were motion-corrected using FSL MCFLIRT and filtering signal drift (high-pass filtering below 0.009 Hz) prior to running subject independent component analysis (ICA) using FSL MELODIC. This initial subject ICA was used to detect noisy signal components from thirty total components per subject. A trained observer labeled noisy components. These components were suppressed using a soft (“non-aggressive”) regression approach, as implemented in FMRIB Software Library (FSL 6.0.3) using `fsl_regfilt` [27]. A low-pass filter ( $>0.12 \text{ Hz}$ ) and spatial smoothing (5 mm FWHM) was then applied to the fMRI scans.

(3) Preprocessed anatomical and fMRI scans were aligned to the MNI152 template (2 mm version). The extracted brain maps were linearly registered to the template using the FSL linear registration tool (FLIRT) [27]. The linear registration output was then nonlinearly warped to the template space using ANTs. Anatomical-to-template linear and nonlinear transformation matrices were applied to fMRI scans at a later stage. Time-series functional images were split into 197 individual volumes, and the first in the series was linearly aligned to the anatomical scan using FLIRT. ANTs were used to warp the lower resolution functional images to their structural counterpart (using a single stage step deformable b-spline syn with a 26-step b-spline distance). (4) Linear and nonlinear warping matrices for fMRI-to-anatomical alignment were applied to individual scans in the time series, then the merged 4D functional time series were moved to the atlas space using the prior anatomical-to-template transformation matrices.

A total of 300 ROI masks, divided into 150 left and 150 right ROIs, were included in our analyses. (5) Nodes were generated under the guidance of the Schaefer 300 functional parcellation [29]. Center voxel coordinates (see above) were used for 3D network visualizations in BrainNet viewer in MATLAB [30]. (6) Signal time series were extracted from preprocessed fMRI scans with the assistance of ROI mask overlays. This generated 300 individual ROI text files per subject that contained L2-normalized resting-state signals as a vector of 197 data points.

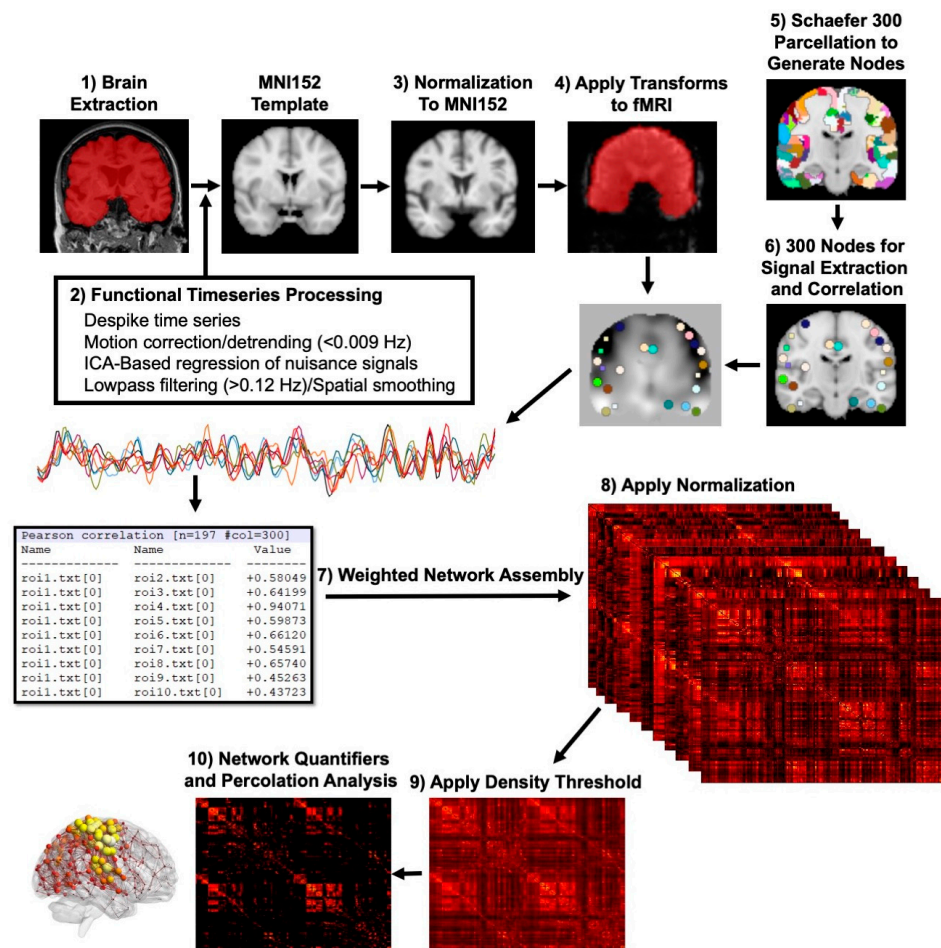


**Figure 1.** Overview of connectomic pipeline from human neuroimaging to network generation. (1) The brain of each subject was extracted using FSL BET. (2) fMRI time series were then despiked, motion-corrected, and detrended. Nuisance signals were removed using ICA-based regression and the signal underwent low-pass filtering and spatial smoothing. (3) Preprocessed anatomical and fMRI scans were aligned to the MNI152 template (2 mm version). (4) Linear and nonlinear warping matrices for fMRI-to-anatomical alignment were applied to individual scans in the time series, then the merged 4D functional time series were moved to the atlas space using the prior anatomical-to-template transformation matrices. (5) Nodes were generated under the guidance of the Schaefer 300 functional parcellation [29]. (6) Signal time series were extracted from preprocessed fMRI scans with the assistance of ROI mask overlays. (7) The time-series files were used in cross-correlations and in calculations of Pearson  $r$  coefficients for every pairwise combination of ROIs (1dCorrelate in AFNI). The resulting matrices were (8) normalized and (9) thresholded across different graph density thresholds (5–30%) to remove spurious edges and negative correlations. Lastly, (10) network quantifiers were calculated, and percolation analysis was conducted.

(7) The time-series files were used in cross-correlations and in calculations of Pearson  $r$  coefficients for every pairwise combination of ROIs (1dCorrelate in AFNI). The resulting number of pairwise correlations was 44,850 per subject (after removing 300 self-correlations). Correlation coefficients were imported to MATLAB and Fisher's transform was applied to ensure a normal distribution of  $z$  values prior to analyses. (8) Correlation matrices were then normalized in MATLAB from zero to one. (9) Matrices were thresholded across different graph density thresholds (5–30%) to remove spurious edges and negative correlations. That is, for example, in the normalization step, all values are rescaled to the range  $[-1, 1]$ , and in thresholding, all values that fall below the threshold are turned to 0 (e.g., for 5% threshold, all values less than 0.95 are removed).



### 2.3. Connectivity Matrix Analysis and Graph Theory Methodology

#### 2.3.1. Group-Average and Null Matrix Generation

In addition to individual-level analysis, percolation theory analysis (detailed in Section 2.3.3) was performed on group-average-level data and null models. To generate group-average matrices, all human ( $n = 51$ ) and mice ( $n = 17$ ) matrices were averaged before thresholding. To generate the null model, “null\_model\_und\_sign [31]” in the Brain Connectivity Toolbox [2] in MATLAB (9.10.0.1739362 (R2021a) Update 5) was used to randomize pre- and post-thresholded group-average human data with a 0.1 frequency of weight sorting.

It is worth mentioning that the choice of a null model when exploring brain network properties has been shown to affect the results and conclusions obtained [32,33]. Null models should be used when examining network properties to assess if the expected brain network property occurs at a rate higher than chance [34]. Null-model choice can impact different normalized measures including path length, small-worldness, and clustering [33]. Therefore, when looking at network properties, null-model choice should be judiciously selected to match the network properties that are influenced by the analysis [35].

For example, in the case of percolation analysis, the most important network properties are degree [36] and strength [37] distributions since the scale of the network plays a role in how it responds to percolations [38,39]. Therefore, we chose to implement Rubinov and Sporns’ null model that maintains degree distribution, strength distribution, and graph density by rewiring edges from an input matrix (group-averaged human data) [31]. Additionally, pre- and post-thresholded matrices were used as input matrices to understand if the thresholding process modifies the null model. Lastly, the correlation coefficient was used to compare strength distributions between the input matrix and the null model [40–42] to ensure the null model matched the strength distribution. In both null-model methods, the correlation coefficient was greater than 0.99, indicating the null model matched the strength distribution of the human data.

#### 2.3.2. Graph Theory Measures

(10) Weighted nodal quantifiers were calculated using the Brain Connectivity Toolbox [2] in MATLAB (9.10.0.1739362 (R2021a) Update 5) to create different attack schemes. Detailed explanations for the six measures used (clustering coefficient [43,44], degree centrality [2], eigenvector centrality [45], local efficiency [46], participation coefficient [47], and strength [2]) can be found within their respective references, since they do not have a major role in this work compared to betweenness centrality. Betweenness centrality (BC) [48] (Brain Connectivity Toolbox’s “betweenness\_wei”) [2] quantifies the fraction of shortest paths that flow through each node in the network. BC is represented by the following equation:

$$b_i = \sum_{h \neq j, h \neq i, j \neq i} \frac{\rho_{hj}(i)}{\rho_{hj}} \quad (1)$$

where  $\rho_{hj}(i)$  is the shortest path between nodes  $h$  and  $j$  that passes through node  $i$  and  $\rho_{hj}$  is the number of shortest paths between nodes  $h$  and  $j$ . The shortest path is important for network function, since it represents how information will flow most efficiently throughout the network.

Alongside nodal measures calculated for attack schemes, two additional modularity measures were explored: Newman’s modularity [3] and rich-club identification [49–51]. Newman’s modularity (Brain Connectivity Toolbox’s “modularity\_und”) [2], identifying non-overlapping modules by comparing within to between module connectivity, was calculated using the following equation:

$$Q^W = \frac{1}{l^W} \sum_{i,j \in N} \left[ w_{ij} - \frac{k_i^W k_j^W}{l^W} \right] \delta_{m_i, m_j}, \quad (2)$$

where  $l^W$  is the sum of all weights in the network,  $w_{ij}$  is the connection between node  $i$  and node  $j$ ,  $k$  is the degree of the node in the network,  $m_i$  and  $m_j$  are the modules containing nodes  $i$  and  $j$ , respectively,  $\delta_{m_i, m_j} = 1$  if  $m_i = m_j$ , and 0 otherwise.

Rich-club organization (Brain Connectivity Toolbox's "rich\_club\_wu") [2], organizes the network into three categories: rich-club nodes, feeder nodes, and local nodes. Rich-club nodes, which are high-degree nodes that are densely connected to other high-degree nodes, are connected to local nodes, or low-degree nodes, through feeder nodes. For weighted networks, the following equation also incorporates edge strength:

$$\phi^W(k) = \frac{W_{>k}}{\sum_{l=1}^{E_{>k}} w_l^{\text{ranked}}}, \quad (3)$$

where  $W_{>k}$  is the sum of weights in the subnetwork  $N_{>k}$  by  $N_{>k}$ ,  $k$  is degree centrality, and  $1 \leq l \leq E$  is the ranked weights of the edges of the matrix. The rich-club coefficient is then normalized against the rich-club coefficient of a random network. The random network was derived using the same null process described above.

### 2.3.3. Percolation Theory Framework

(10) Using the previously mentioned nodal quantifiers, brain networks were analyzed using percolation theory through the targeted removal of nodes based on an iteratively calculated nodal quantifier. First, in each attack scheme, a nodal quantifier was calculated for all nodes across the network. Next, the node with the highest value had all connections changed to zero, representing removal from the network. Lastly, the largest cluster size, or the largest fully connected component of the network, was measured. This process was repeated until all nodes were removed from the network, resulting in a completely disconnected network.

Alongside the seven quantifier-based attacks, two additional attack schemes were implemented: random and collective influence. In the random attacks, nodes are removed using MATLAB's pseudorandom number generator produced by the "randi" function. The collective influence attack scheme utilizes an optimized percolation method through energy minimization to break apart network components [52,53]. Collective influence was calculated using ComplexCi in C++ [54]. While collective influence identifies optimal percolation pathways, it is important to note that it has no quantifiable value outside of network percolation.

### 2.3.4. Module Identification Using Percolation Theory

Similarly to calculating the largest cluster size after each attack, the betweenness centrality of every node was iteratively calculated and then averaged to create an average betweenness centrality for the network. When plotting the average betweenness centrality and largest cluster size against the fraction of attacks, large phase transitions, or decreases in largest cluster size, are preceded by spikes in average betweenness centrality.

Alongside calculating the largest cluster and average betweenness centrality, the resulting matrix after each attack is saved. Cluster size groupings can then be calculated using Brain Connectivity Toolbox's "get\_components" on the resulting matrix immediately after the phase transition [2]. The nodes within the two largest cluster sizes are thus the terminal modules, while any removed nodes are classified as the transfer module.

Disconnected nodes, either from higher thresholds or small breaks in network components, can either be omitted or arbitrarily included in any module, preferably the transfer module. Additionally, the choice of which phase transition to utilize when identifying modules is arbitrary. In this work, average betweenness centrality spikes with the largest accompanying drop in the largest cluster size were examined, but other methods utilizing the largest spike in average betweenness centrality are equally valid. Phase transition modules were visualized using BrainNet Viewer [30], a graphical tool to visualize brain networks, via a surface mesh version of the MNI152 template.

### 3. Results

While previous studies have explored percolation theory applied to brain networks, our novel perspective examines a significant decrease in brain network cluster size as a potential phase transition. Large drops in cluster size due to a single attack represent a module being removed from the network since a single attack should only reduce the largest cluster size by one. While nine different types of attacks were tested (Supplementary Figure S1), BC demonstrated a noticeably larger phase transition. BC quantifies how often a node lies within the shortest paths in a network. Thus, removing nodes based on BC removes nodes required for optimal communication between modules in the brain. This is supported by BC attacks degrading brain networks at the fastest rate (fewest attacks) [6] (Supplementary Figure S1). The expedited degradation is incremental rather than gradual, indicating that BC attacks optimally degrade the network to separate large functional modules from the core of the network. This incremental degradation demonstrates phase-transition behavior from a supercritical regime or a fully connected network to a subcritical regime composed of smaller clusters, as seen by the large drop-off in cluster size (Figure 2). Subsequent drops in cluster size indicate further sub-modules identified by this method, which can be optimized to select a desired number of modules, similar to previous modularity algorithms [3,49,55].

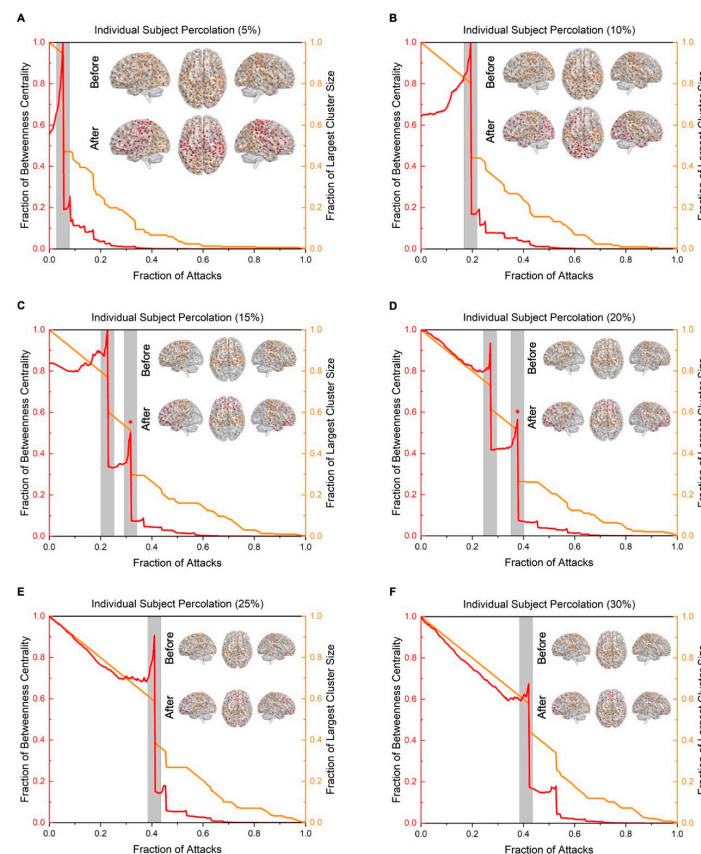


**Figure 2.** Individual-level subject percolation showing the average betweenness centrality spike coinciding with a significant drop in the largest cluster across different thresholds (5–30%). The gray shaded area represents the phase transition through the critical point. Plots with two gray shaded areas represent thresholds that have two potential phase transitions. The shaded area with the red asterisk is the phase transition shown in the brain inset. In the brain inset, the orange nodes show nodes part of the largest clusters while the red nodes in the after image are completely disconnected from the orange cluster. As seen throughout different thresholds, the regions identified from the phase transitions are relatively consistent, with one region located near the central gyrus and the subsequent region located in the anterior and posterior parts of the brain.

This network phase transition, or large drop in cluster size, can also be identified by peaks in average BC for the network. Figure 2 shows the average BC and cluster size plotted against the number of attacks at a series of thresholds. Each peak in average BC demonstrates a localized critical point, and the largest peak demonstrates a global critical point whereby the network is degraded the most. A spike in average BC signifies a single path, or node, for information to flow between two hubs. However, looking at the maximum nodal BC versus attacks does not always convey a decrease in cluster size due to spurious peaks in maximum nodal BC. This discrepancy between average BC and maximum nodal BC is due to the ability for a node not to be a critical one but still have a relatively high BC compared to other nodes in the network.

These results are consistent across different connectomic networks, including networks derived from fMRI of mouse brains (Supplementary Figures S2 and S3), null models generated from human data (Supplementary Figures S4 and S5), and group-average level networks (Supplementary Figures S6 and S7); however, phase transitions are considerably less pronounced in both null models (excluding 15% post-threshold null model) and group-average mouse models. The comparison against null models is particularly important, since they have the same degree/strength distribution as a human network (correlation coefficient greater than 0.99), thus meaning the spiking and phase transition is most likely a feature of brain network organization. Moreover, it is well known that one limitation within connectomics is the reliance on choosing a threshold for networks to minimize spurious edges while reducing the removal of true correlations, impacting network quantifiers and community structures. Remarkably however, this phase transition methodology, including the BC spike prediction, works across numerous thresholds with just a few differences. As the network threshold decreases, the phase transition and BC peak occur at a higher fraction of attacks. Additionally, different thresholds have a different number of phase transitions. High (Figure 2A,B) and low (Figure 2E,F) thresholds have a single phase transition indicated by a single large peak, while in-between thresholds (Figure 2C,D) have dual-phase transitions indicated by two large peaks. With lower thresholds, the phase transition understandably appears at later attacks given the greater number of connections overall, yet the community structures are relatively consistent across thresholds (Figure 2). Even at significantly different thresholds (5% Figure 2A and 30% Figure 2F), the phase transition results in two existing modules, one near the central gyrus and a second in both the anterior and posterior of the brain. In the case of more than one phase transition, the choice of phase transition determines how many nodes are included in the transfer module as opposed to the terminal modules.

The ability to identify modules using a BC phase transition lens allows for the identification of unique functional components of brain networks. To illustrate this, Figure 3 shows different modularity measures for an individual subject compared against the phase transition modularity described in this work at a 10% graph density threshold. Figure 3A shows an example of connectivity matrix analysis that visualizes connections present between each node. The matrices are colored by modules found using the phase transition modularity method, with black denoting no connections found at the node-to-node edge. Nodes (x and y axes) are rearranged based on different modularity methods with the module denoted on the right-hand side; however, within-module node rearrangement is arbitrary. The functional atlas used to generate the brain networks results in one dense cluster in the visual network with more sparsely interconnected regions across the brain (Figure 3B). Both rich-club modularity (Figure 3C) [49–51] and Newman’s modularity (Figure 3D) [3] show modules that contain nodes that have connections across numerous modules. Thus, the functional brain atlas (Figure 3B), rich-club modularity (Figure 3C), and Newman’s modularity (Figure 3D) all create dependent modules, since modules contain nodes that connect across numerous other modules. In contrast, phase transition modularity resulted in three distinct modules, two completely independent of each other (Figure 3E). Specifically, two modules from splitting the largest cluster and one module composed of the removed nodes. The two modules generated from the cluster, which will be denoted as



terminal modules, are only connected to each other through the third removed module, or transfer module. No other modularity measure creates fully independent modules shown by the lack of connections between the two terminal modules (Figure 3E).

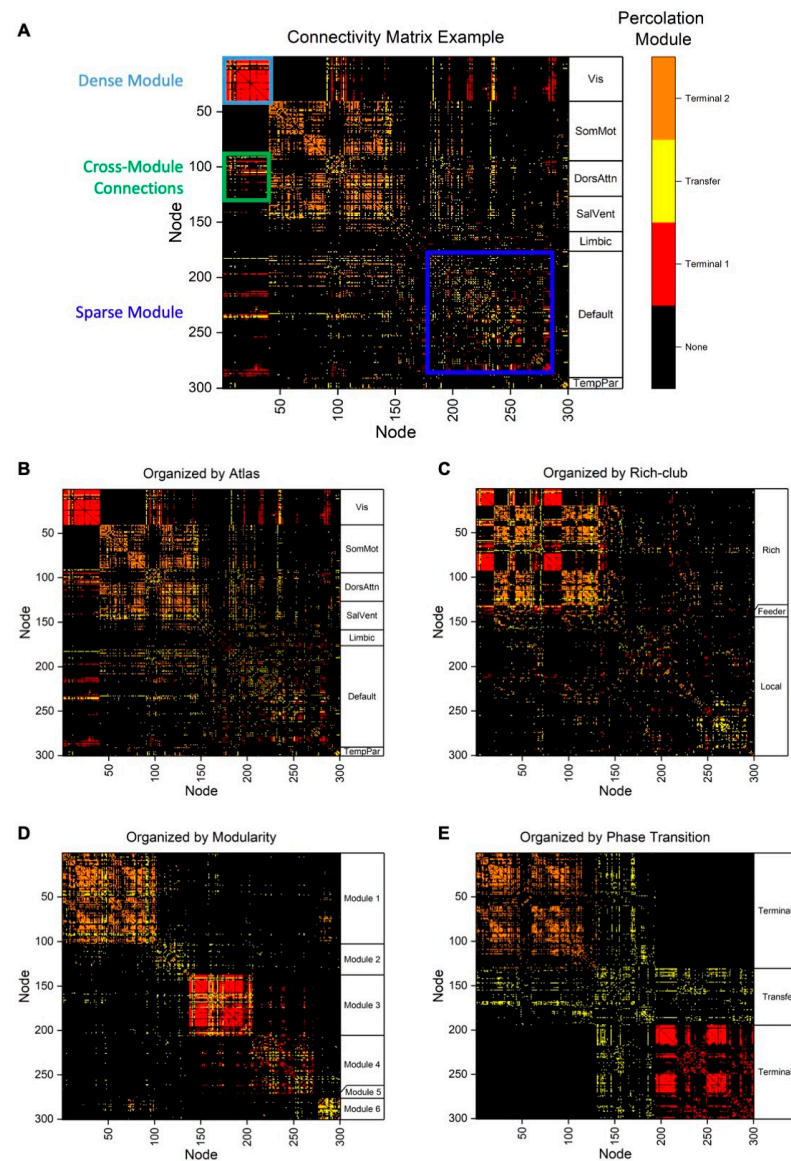


**Figure 3.** (A) Representative connectivity matrix example illustrating key features shown by the following heatmaps from an individual subject. Nodes (x and y axes) are rearranged based on different modularity methods with the module denoted on the right-hand side; however, within-module node rearrangement is arbitrary. The matrices are colored by modules found using the phase transition modularity method, with black denoting no connections found at the node-to-node edge. Connections near the diagonal (light and navy blue) represent dense and sparse module connectivity, respectively. Off-diagonal clusters (green) represent between-module connections. Vis: visual; SomMot: somatomotor; DorsAttn: dorsal attention; SalVent: salience/ventral attention; TempPar: temporoparietal. (B) Connectivity matrix organized by the Schaefer 300 node functional parcellation [29] used to create the original connectivity matrices. (C) Connectivity matrix organized by identifying features of the rich club: rich nodes, feeder nodes, and local nodes [49–51]. (D) Connectivity matrix organized by Newman's modularity [3]. (E) Connectivity matrix organized by phase transition modularity. The large black squares demonstrate the reliance on the transfer module (yellow) to connect the terminal modules.

#### 4. Discussion

The phase transition behavior of the brain networks in response to betweenness centrality percolations can provide insight into brain resilience and optimization. Brain networks were highly vulnerable to BC attacks (Figure 2 and Figure S6) which has been shown in previous research [6,14]. However, the associated phase transition preceded by a spike in average BC demonstrates the functional trade-off of relying on being near a phase transition for optimal processing [56,57]. Recent work has demonstrated healthy brains lie at a near-critical threshold, rather than exactly at a critical point [56]. Remaining at a near-critical point is believed to balance computational efficiency and global dynamics. While many biological research efforts have looked at local criticality through neuronal spiking [58], criticality can also be examined at the global level through brain networks. This present work supports the hypothesis that the brain functions at a near-critical state, demonstrated by the percentage of attacks needed before a phase transition (significant drop in cluster size). If brain networks were maintained at a critical point, it would only take a small number of attacks to produce the phase transition. While this occurs at very high thresholds ( $\leq 2\%$ ), lower thresholds require a larger number of attacks to reach this phase transition (Figure 2), demonstrating a near-critical nature rather than strictly lying at a critical point. This distance, or number of attacks, to a critical point may for example serve as a biomarker for neurodegeneration while providing an indication of robustness against neurodegeneration before significant clinical or functional symptomatology is present.

This phase transition signified by the BC spike could also be used to support the critical brain hypothesis. The critical brain hypothesis states the brain functions near a phase transition boundary, or on the edge of chaos, for optimal processing [56]. Support for this theory has been found from microscale spike recordings [58] to macroscale neuroimaging such as fMRI [59,60]. Evidence has also been found in the connectomic analysis of neuromorphic hardware [61]. However, criticism of the theory stems from the complicated definition of “criticality” and where the brain lies on the spectrum of criticality. It is important to stress that in this work, criticality is defined as the connectedness of the network as a unit, or largest cluster. While this definition fits within the bounds of traditional percolation theory regarding crystal structure, it does limit the quantifiability of “chaos.” For example, typical neural network processing measures such as Poincare and Lyapunov exponents cannot be utilized since the data are not defined with respect to time, but with respect to the number of nodes removed [62].

This phase transition modularity also offers a unique lens to view brain modularity through transfer and terminal hubs. This modularity configuration of transfer modules has been proposed in previous work [63]. Similarly, rich-club modularity, which has been widely used across connectomic studies [49–51], uses a similar idea whereby feeder nodes connect non-rich-club nodes to the central rich club. However, instead of individual feeder nodes, this work categorizes nodes critical for information flow between modules as a module itself. This modularity perspective aligns with a neural network framework where the terminal modules act as input and output layers and the information transfer module acts as a hidden layer connecting them.

Therefore, one potential application of the phase transition modularity is quantifiably translating brain networks into neural networks (Figure 4). While previous efforts have used connectome networks to generate neural networks [64], this method provides a definitive mapping or allocation of nodes to specific neural network layers. The transfer module can define the hidden layer, and the two other modules, or terminal modules, can act as pseudo-input/output layers, with one terminal module functioning as the input layer and the other as the output layer. It is worth noting that while these terminal layers are interchangeable between input and output layers, the most important finding is the necessity of the transfer module to communicate between the two terminal modules. For example, this network configuration can then input into connectome-based computing software, such as conn2res [65], to simulate reservoir computing based on human fMRI.

This neural network configuration thus enables the quantification of the processing power of the connectome network using clearly defined modules through percolation theory.

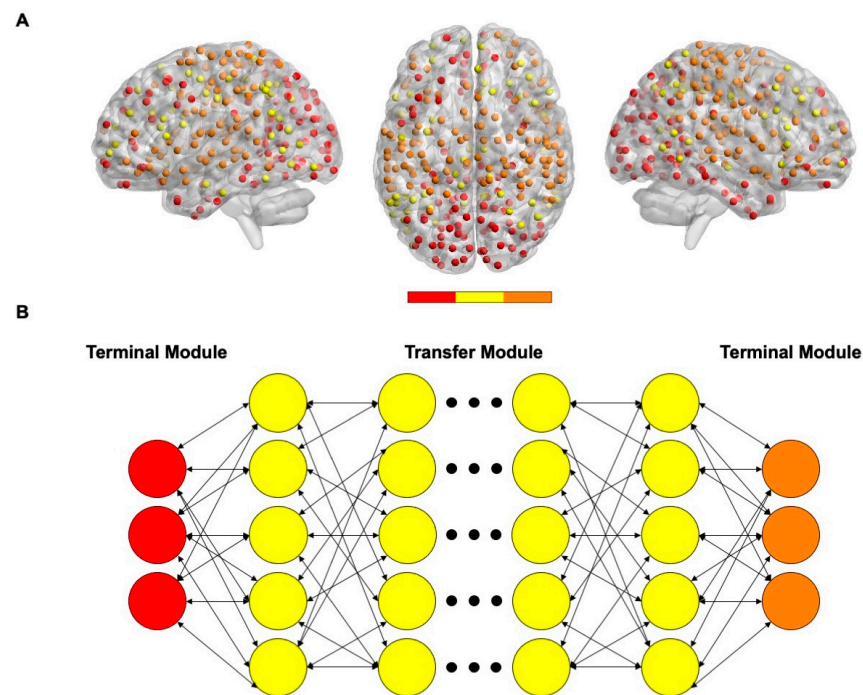


**Figure 4.** (A) Visual representation of the modules identified using individual-level subject percolation. The red and orange nodes represent nodes part of their respective terminal module, while the yellow nodes represent nodes in the transfer module. (B) Neural network representation as a potential application of phase transition modularity. Transfer modules identified using phase transition modularity can act as hidden layers, while terminal layers function as either input or output layers.

This work does have some inherent limitations. It is known that the field of connectomics has limitations regarding atlas choice. The atlas chosen can influence the community structures identified using percolation modularity; however, as shown using null models and mouse data, this methodology works regardless of network construction methods. Additionally, this methodology only identified three functional hubs in the brain, as opposed to other modularity algorithms identifying smaller clusters. However, the goal of this work, rather than exclusively identifying modules in the brain that correspond to a specific function, also includes using a new perspective to translate fMRI into a neural network. Thus, three modules fit within the schema of neural networks, including three general layers: input, output, and hidden. Specific to this work is one possible limitation to the widespread practical application of this methodology, the run time, since betweenness centrality is a computationally expensive algorithm that increases in run time with increasing network size. However, specifically for brain networks and connectomics, atlases used to generate connectivity matrices often have fewer than 400 nodes [66]. This work, using 300 nodes, had run times of around four minutes (MacBook Pro 2019 (Apple, Cupertino, CA, USA), 2.6 GHz 6-Core Intel Core i7 (Intel, Santa Clara, CA, USA), 16 GM 2667 MHz DDR4 (SK HYNIX, Icheon, Republic of Korea), AMD Radeon Pro 5300M 4 GB (AMD, Santa Clara, CA, USA), Intel UHD Graphics 630 1536 MG) for each subject at our lowest typical threshold (40%), demonstrating this methodology is useful and time-effective for brain modularity analysis and is far less computationally expensive than small-worldness or rich-club analysis, which requires null networks [49–51]. Additionally, our findings may be a result of general network properties that may not be specific to brain networks [32,33]; however, the less pronounced phase transition found in null models that control for degree and strength

distribution indicate this is most likely a feature of brain networks. An important note is that while our null model controls for network aspects that have been previously shown to be important for percolation response [36–39], it may not control for every property that is important for the percolation modularity and betweenness centrality spiking in this work. More complex and conservative null models are currently being developed that may provide better insight and comparison to our current work [32]. Thus, future work can explore this percolation modularity and betweenness centrality phenomenon with more extensive null models to enhance the comparative analysis. Lastly, our data include exclusively elderly (ages 70–95) human participants, which may impact generalizability; however, the inclusion of both human and mouse data lend increased generatability to cross-species brain network analysis.

## 5. Conclusions

This work explores brain connectomics and modularity through a phase transition and criticality lens. Our work shows a novel brain modularity methodology that can identify community structures by implementing percolation theory with betweenness centrality that works across species (human, mice) and null networks. Additionally, we provide further evidence of the brain functioning at a near-critical state predicted by a peak in average betweenness centrality, with implications for neural networks, neuromorphic architecture, and neurodegenerative diseases. Future work should explore this phase transition and near-critical behavior through an energy/cost minimization lens while also elucidating reasons for differences in spiking across networks through comparisons to more complex null models and degree/strength distributions. Additionally, longitudinal connectomic analysis of patients with neurodegenerative diseases should explore if the trend in rising average betweenness centrality can be a predictive factor for cognitive decline.

**Supplementary Materials:** The following supporting information can be downloaded at <https://www.mdpi.com/article/10.3390/app14104197/s1>. Figure S1: Largest cluster size in response to various targeted attacks; Figure S2: Individual-level mouse percolation; Figure S3: Group-average mouse percolation; Figure S4: Null-model percolation (pre-threshold); Figure S5: Null-model percolation (post-threshold); Figure S6: Group-average percolation; Figure S7: Connectivity matrices derived from group-average connectivity matrices at 10% threshold.

**Author Contributions:** Conceptualization, P.K. and J.C.N.; methodology, P.K. and M.F.; software, P.K.; validation, P.K.; formal analysis, P.K.; investigation, P.K.; resources, M.F. and J.C.N.; data curation, M.F.; writing—original draft preparation, P.K.; writing—review and editing, P.K., M.F. and J.C.N.; visualization, P.K., M.F. and J.C.N.; supervision, M.F. and J.C.N.; funding acquisition, J.C.N. All authors have read and agreed to the published version of the manuscript.

**Funding:** This work was supported by the University of Florida with a AI2020 Catalyst Grant (AWD09459). Any opinions, findings, conclusions, or recommendations expressed in this material are those of the authors and do not necessarily reflect the views of the University of Florida. Data collection and sharing for the Alzheimer’s Disease Neuroimaging Initiative (ADNI) is funded by the National Institute on Aging (National Institutes of Health Grant U19 AG024904). The grantee organization is the Northern California Institute for Research and Education. In the past, ADNI has also received funding from the National Institute of Biomedical Imaging and Bioengineering, the Canadian Institutes of Health Research, and private sector contributions through the Foundation for the National Institutes of Health (FNIH) including generous contributions from the following: AbbVie, Alzheimer’s Association; Alzheimer’s Drug Discovery Foundation; Araclon Biotech; BioClinica, Inc.; Biogen; Bristol-Myers Squibb Company; CereSpir, Inc.; Cogstate; Eisai Inc.; Elan Pharmaceuticals, Inc.; Eli Lilly and Company; EuroImmun; F. Hoffmann-La Roche Ltd and its affiliated company Genentech, Inc.; Fujirebio; GE Healthcare; IXICO Ltd.; Janssen Alzheimer Immunotherapy Research & Development, LLC.; Johnson & Johnson Pharmaceutical Research & Development LLC.; Lumosity; Lundbeck; Merck & Co., Inc.; Meso Scale Diagnostics, LLC.; NeuroRx Research; Neurotrack Technologies; Novartis Pharmaceuticals Corporation; Pfizer Inc.; Piramal Imaging; Servier; Takeda Pharmaceutical Company; and Transition Therapeutics. The funder had no involvement in the study methodology, analysis, or results.



**Institutional Review Board Statement:** The study was conducted in accordance with the Declaration of Helsinki, and approved by the Institutional Review Board of the University of Florida (IRB201901878) (11 July 2019). The animal study protocol was approved by the Institutional Review Board of the University of Florida.

**Informed Consent Statement:** Informed consent was obtained from all subjects involved in the study.

**Data Availability Statement:** Requests for mouse data should be forwarded to the original data author, Colon-Perez et al. [24]. Human data are available from the ADNI repository ([ida.loni.usc.edu](http://ida.loni.usc.edu)).

**Conflicts of Interest:** The authors declare no conflicts of interest.

## References

1. Milano, M.; Guzzi, P.H.; Cannataro, M. Network building and analysis in connectomics studies: A review of algorithms, databases and technologies. *Netw. Model. Anal. Health Inform. Bioinform.* **2019**, *8*, 13. [\[CrossRef\]](#)
2. Rubinov, M.; Sporns, O. Complex network measures of brain connectivity: Uses and interpretations. *NeuroImage* **2010**, *52*, 1059–1069. [\[CrossRef\]](#)
3. Newman, M.E.J. Modularity and community structure in networks. *Proc. Natl. Acad. Sci. USA* **2006**, *103*, 8577–8582. [\[CrossRef\]](#)
4. Sporns, O.; Betzel, R.F. Modular Brain Networks. *Annu. Rev. Psychol.* **2016**, *67*, 613–640. [\[CrossRef\]](#)
5. Warsi, N.M.; Wong, S.M.; Germann, J.; Boutet, A.; Arski, O.N.; Anderson, R.; Erdman, L.; Yan, H.; Suresh, H.; Gouveia, F.V.; et al. Dissociable default-mode subnetworks subserve childhood attention and cognitive flexibility: Evidence from deep learning and stereotactic electroencephalography. *Neural Netw.* **2023**, *167*, 827–837. [\[CrossRef\]](#)
6. Kotlarz, P.; Nino, J.C.; Febo, M. Connectomic analysis of Alzheimer’s disease using percolation theory. *Netw. Neurosci.* **2022**, *6*, 213–233. [\[CrossRef\]](#)
7. Tao, Y.; Rapp, B. Investigating the network consequences of focal brain lesions through comparisons of real and simulated lesions. *Sci. Rep.* **2021**, *11*, 2213. [\[CrossRef\]](#)
8. Razban, R.M.; Pachter, J.A.; Dill, K.A.; Mujica-Parodi, L.R. Early path dominance as a principle for neurodevelopment. *Proc. Natl. Acad. Sci. USA* **2023**, *120*, e2218007120. [\[CrossRef\]](#)
9. Achard, S.; Salvador, R.; Whitcher, B.; Suckling, J.; Bullmore, E. A Resilient, Low-Frequency, Small-World Human Brain Functional Network with Highly Connected Association Cortical Hubs. *J. Neurosci.* **2006**, *26*, 63–72. [\[CrossRef\]](#) [\[PubMed\]](#)
10. Kaiser, M.; Martin, R.; Andras, P.; Young, M.P. Simulation of robustness against lesions of cortical networks. *Eur. J. Neurosci.* **2007**, *25*, 3185–3192. [\[CrossRef\]](#) [\[PubMed\]](#)
11. Lynall, M.-E.; Bassett, D.S.; Kerwin, R.; McKenna, P.J.; Kitzbichler, M.; Muller, U.; Bullmore, E. Functional connectivity and brain networks in schizophrenia. *J. Neurosci. Off. J. Soc. Neurosci.* **2010**, *30*, 9477–9487. [\[CrossRef\]](#)
12. Cabral, J.; Hugues, E.; Kringelbach, M.L.; Deco, G. Modeling the outcome of structural disconnection on resting-state functional connectivity. *NeuroImage* **2012**, *62*, 1342–1353. [\[CrossRef\]](#)
13. Joyce, K.E.; Hayasaka, S.; Laurienti, P.J. The Human Functional Brain Network Demonstrates Structural and Dynamical Resilience to Targeted Attack. *PLoS Comput. Biol.* **2013**, *9*, e1002885. [\[CrossRef\]](#)
14. Guo, S.; Chen, X.; Liu, Y.; Kang, R.; Liu, T.; Li, D. Percolation Analysis of Brain Structural Network. *Front. Phys.* **2021**, *9*, 698077. [\[CrossRef\]](#)
15. Mastrandrea, R.; Piras, F.; Gabrielli, A.; Banaj, N.; Caldarelli, G.; Spalletta, G.; Gili, T. The unbalanced reorganization of weaker functional connections induces the altered brain network topology in schizophrenia. *Sci. Rep.* **2021**, *11*, 15400. [\[CrossRef\]](#)
16. Langton, C.G. Computation at the edge of chaos: Phase transitions and emergent computation. *Phys. Nonlinear Phenom.* **1990**, *42*, 12–37. [\[CrossRef\]](#)
17. Bertschinger, N.; Natschläger, T. Real-Time Computation at the Edge of Chaos in Recurrent Neural Networks. *Neural Comput.* **2004**, *16*, 1413–1436. [\[CrossRef\]](#)
18. Gao, J.; Barzel, B.; Barabási, A.-L. Universal resilience patterns in complex networks. *Nature* **2016**, *530*, 307–312. [\[CrossRef\]](#)
19. Dong, G.; Wang, F.; Shekhtman, L.M.; Danziger, M.M.; Fan, J.; Du, R.; Liu, J.; Tian, L.; Stanley, H.E.; Havlin, S. Optimal resilience of modular interacting networks. *Proc. Natl. Acad. Sci. USA* **2021**, *118*, e1922831118. [\[CrossRef\]](#) [\[PubMed\]](#)
20. Cohen, R.; Erez, K.; ben-Avraham, D.; Havlin, S. Resilience of the Internet to Random Breakdowns. *Phys. Rev. Lett.* **2000**, *85*, 4626–4628. [\[CrossRef\]](#) [\[PubMed\]](#)
21. Aerts, H.; Fias, W.; Caeyenberghs, K.; Marinazzo, D. Brain networks under attack: Robustness properties and the impact of lesions. *Brain* **2016**, *139*, 3063–3083. [\[CrossRef\]](#)
22. Stanford, W.C.; Mucha, P.J.; Dayan, E. A robust core architecture of functional brain networks supports topological resilience and cognitive performance in middle- and old-aged adults. *Proc. Natl. Acad. Sci. USA* **2022**, *119*, e2203682119. [\[CrossRef\]](#)
23. Crossley, N.A.; Mechelli, A.; Scott, J.; Carletti, F.; Fox, P.T.; McGuire, P.; Bullmore, E.T. The hubs of the human connectome are generally implicated in the anatomy of brain disorders. *Brain* **2014**, *137*, 2382–2395. [\[CrossRef\]](#) [\[PubMed\]](#)
24. Colon-Perez, L.M.; Ibanez, K.R.; Suarez, M.; Torroella, K.; Acuna, K.; Ofori, E.; Levites, Y.; Vaillancourt, D.E.; Golde, T.E.; Chakrabarty, P.; et al. Neurite orientation dispersion and density imaging reveals white matter and hippocampal microstructure

- changes produced by Interleukin-6 in the TgCRND8 mouse model of amyloidosis. *NeuroImage* **2019**, *202*, 116138. [[CrossRef](#)] [[PubMed](#)]
25. Sahara, N.; Perez, P.D.; Lin, W.-L.; Dickson, D.W.; Ren, Y.; Zeng, H.; Lewis, J.; Febo, M. Age-related decline in white matter integrity in a mouse model of tauopathy: An in vivo diffusion tensor magnetic resonance imaging study. *Neurobiol. Aging* **2014**, *35*, 1364–1374. [[CrossRef](#)]
  26. Cox, R.W. AFNI: Software for Analysis and Visualization of Functional Magnetic Resonance Neuroimages. *Comput. Biomed. Res.* **1996**, *29*, 162–173. [[CrossRef](#)] [[PubMed](#)]
  27. Jenkinson, M.; Bannister, P.; Brady, M.; Smith, S. Improved Optimization for the Robust and Accurate Linear Registration and Motion Correction of Brain Images. *NeuroImage* **2002**, *17*, 825–841. [[CrossRef](#)] [[PubMed](#)]
  28. Klein, A.; Andersson, J.; Ardekani, B.A.; Ashburner, J.; Avants, B.; Chiang, M.-C.; Christensen, G.E.; Collins, D.L.; Gee, J.; Hellier, P.; et al. Evaluation of 14 nonlinear deformation algorithms applied to human brain MRI registration. *NeuroImage* **2009**, *46*, 786–802. [[CrossRef](#)] [[PubMed](#)]
  29. Schaefer, A.; Kong, R.; Gordon, E.M.; Laumann, T.O.; Zuo, X.-N.; Holmes, A.J.; Eickhoff, S.B.; Yeo, B.T.T. Local-Global Parcellation of the Human Cerebral Cortex from Intrinsic Functional Connectivity MRI. *Cereb. Cortex* **2018**, *28*, 3095–3114. [[CrossRef](#)]
  30. Xia, M.; Wang, J.; He, Y. BrainNet Viewer: A Network Visualization Tool for Human Brain Connectomics. *PLoS ONE* **2013**, *8*, e68910. [[CrossRef](#)]
  31. Rubinov, M.; Sporns, O. Weight-conserving characterization of complex functional brain networks. *NeuroImage* **2011**, *56*, 2068–2079. [[CrossRef](#)] [[PubMed](#)]
  32. Váša, F.; Mišić, B. Null models in network neuroscience. *Nat. Rev. Neurosci.* **2022**, *23*, 493–504. [[CrossRef](#)] [[PubMed](#)]
  33. Hosseini, S.M.H.; Kesler, S.R. Influence of Choice of Null Network on Small-World Parameters of Structural Correlation Networks. *PLoS ONE* **2013**, *8*, e67354. [[CrossRef](#)] [[PubMed](#)]
  34. Chung, J.; Bridgeford, E.; Arroyo, J.; Pedigo, B.D.; Saad-Eldin, A.; Gopalakrishnan, V.; Xiang, L.; Priebe, C.E.; Vogelstein, J.T. Statistical Connectomics. *Annu. Rev. Stat. Its Appl.* **2021**, *8*, 463–492. [[CrossRef](#)]
  35. Fornito, A.; Zalesky, A.; Bullmore, E.T. (Eds.) Chapter 10—Null Models. In *Fundamentals of Brain Network Analysis*; Academic Press: San Diego, CA, USA, 2016; pp. 355–381. ISBN 978-0-12-407908-3.
  36. Breskin, I.; Soriano, J.; Moses, E.; Tlusty, T. Percolation in Living Neural Networks. *Phys. Rev. Lett.* **2006**, *97*, 188102. [[CrossRef](#)]
  37. Kong, L.-W.; Li, M.; Liu, R.-R.; Wang, B.-H. Percolation on networks with weak and heterogeneous dependency. *Phys. Rev. E* **2017**, *95*, 032301. [[CrossRef](#)] [[PubMed](#)]
  38. Callaway, D.S.; Newman, M.E.J.; Strogatz, S.H.; Watts, D.J. Network Robustness and Fragility: Percolation on Random Graphs. *Phys. Rev. Lett.* **2000**, *85*, 5468–5471. [[CrossRef](#)] [[PubMed](#)]
  39. Cohen, R.; ben-Avraham, D.; Havlin, S. Percolation critical exponents in scale-free networks. *Phys. Rev. E* **2002**, *66*, 036113. [[CrossRef](#)]
  40. Fisher, R.A. *Statistical Methods for Research Workers*, 13th ed.; Rev. in Biological monographs and manuals; Hafner: New York, NY, USA, 1958.
  41. Kendall, M.; Stuart, A. *The Advanced Theory of Statistics. Volume 2: Inference and Relationship*, 4th ed.; Macmillan: New York, NY, USA, 1979; ISBN 978-0-02-847820-3.
  42. Press, W.H.; Flannery, B.P.; Teukolsky, S.A.; Vetterling, W.T. *Numerical Recipes in C: The Art of Scientific Computing*, 2nd ed.; Cambridge University Press: Cambridge, UK; New York, NY, USA, 1992; ISBN 978-0-521-43108-8.
  43. Onnela, J.-P.; Saramäki, J.; Kertész, J.; Kaski, K. Intensity and coherence of motifs in weighted complex networks. *Phys. Rev. E* **2005**, *71*, 065103. [[CrossRef](#)]
  44. Watts, D.J.; Strogatz, S.H. Collective dynamics of ‘small-world’ networks. *Nature* **1998**, *393*, 440–442. [[CrossRef](#)]
  45. Newman, M.E.J. Mathematics of Networks. In *The New Palgrave Dictionary of Economics*; Palgrave Macmillan: London, UK, 2016; pp. 1–8. ISBN 978-1-349-95121-5.
  46. Latora, V.; Marchiori, M. Efficient Behavior of Small-World Networks. *Phys. Rev. Lett.* **2001**, *87*, 198701. [[CrossRef](#)] [[PubMed](#)]
  47. Guimerà, R.; Amaral, L.A.N. Cartography of complex networks: Modules and universal roles. *J. Stat. Mech. Theory Exp.* **2005**, *2005*, P02001. [[CrossRef](#)] [[PubMed](#)]
  48. Freeman, L.C. Centrality in social networks conceptual clarification. *Soc. Netw.* **1978**, *1*, 215–239. [[CrossRef](#)]
  49. Kim, D.-J.; Min, B.-K. Rich-club in the brain’s macrostructure: Insights from graph theoretical analysis. *Comput. Struct. Biotechnol. J.* **2020**, *18*, 1761–1773. [[CrossRef](#)] [[PubMed](#)]
  50. Opsahl, T.; Colizza, V.; Panzarasa, P.; Ramasco, J.J. Prominence and Control: The Weighted Rich-Club Effect. *Phys. Rev. Lett.* **2008**, *101*, 168702. [[CrossRef](#)] [[PubMed](#)]
  51. van den Heuvel, M.P.; Sporns, O. Rich-Club Organization of the Human Connectome. *J. Neurosci.* **2011**, *31*, 15775–15786. [[CrossRef](#)]
  52. Morone, F.; Makse, H.A. Influence maximization in complex networks through optimal percolation. *Nature* **2015**, *524*, 65–68. [[CrossRef](#)] [[PubMed](#)]
  53. Morone, F.; Min, B.; Bo, L.; Mari, R.; Makse, H.A. Collective Influence Algorithm to find influencers via optimal percolation in massively large social media. *Sci. Rep.* **2016**, *6*, 30062. [[CrossRef](#)] [[PubMed](#)]
  54. Zhu, F. Improved collective influence of finding most influential nodes based on disjoint-set reinsertion. *Sci. Rep.* **2018**, *8*, 14503. [[CrossRef](#)]

55. Hagmann, P.; Cammoun, L.; Gigandet, X.; Meuli, R.; Honey, C.J.; Wedeen, V.J.; Sporns, O. Mapping the Structural Core of Human Cerebral Cortex. *PLoS Biol.* **2008**, *6*, e159. [[CrossRef](#)]
56. O’Byrne, J.; Jerbi, K. How critical is brain criticality? *Trends Neurosci.* **2022**, *45*, 820–837. [[CrossRef](#)] [[PubMed](#)]
57. Zimmern, V. Why Brain Criticality Is Clinically Relevant: A Scoping Review. *Front. Neural Circuits* **2020**, *14*, 565335. [[CrossRef](#)] [[PubMed](#)]
58. Fosque, L.J.; Williams-García, R.V.; Beggs, J.M.; Ortiz, G. Evidence for Quasicritical Brain Dynamics. *Phys. Rev. Lett.* **2021**, *126*, 098101. [[CrossRef](#)] [[PubMed](#)]
59. Fraiman, D.; Balenzuela, P.; Foss, J.; Chialvo, D.R. Ising-like dynamics in large-scale functional brain networks. *Phys. Rev. E* **2009**, *79*, 061922. [[CrossRef](#)] [[PubMed](#)]
60. Jannesari, M.; Saeedi, A.; Zare, M.; Ortiz-Mantilla, S.; Plenz, D.; Benasich, A.A. Stability of neuronal avalanches and long-range temporal correlations during the first year of life in human infants. *Brain Struct. Funct.* **2020**, *225*, 1169–1183. [[CrossRef](#)] [[PubMed](#)]
61. Suárez, L.E.; Richards, B.A.; Lajoie, G.; Misic, B. Learning function from structure in neuromorphic networks. *Nat. Mach. Intell.* **2021**, *3*, 771–786. [[CrossRef](#)]
62. Parker, T.S.; Chua, L.O. *Practical Numerical Algorithms for Chaotic Systems*; Springer: New York, NY, USA, 1989; ISBN 978-1-4612-8121-4.
63. Ito, T.; Kulkarni, K.R.; Schultz, D.H.; Mill, R.D.; Chen, R.H.; Solomyak, L.I.; Cole, M.W. Cognitive task information is transferred between brain regions via resting-state network topology. *Nat. Commun.* **2017**, *8*, 1027. [[CrossRef](#)]
64. Ito, T.; Yang, G.R.; Laurent, P.; Schultz, D.H.; Cole, M.W. Constructing neural network models from brain data reveals representational transformations linked to adaptive behavior. *Nat. Commun.* **2022**, *13*, 673. [[CrossRef](#)] [[PubMed](#)]
65. Suárez, L.E.; Mihalik, A.; Milisav, F.; Marshall, K.; Li, M.; Vértes, P.E.; Lajoie, G.; Misic, B. Connectome-based reservoir computing with the conn2res toolbox. *Nat. Commun.* **2024**, *15*, 656. [[CrossRef](#)]
66. Albers, K.J.; Ambrosen, K.S.; Liptrot, M.G.; Dyrby, T.B.; Schmidt, M.N.; Mørup, M. Using connectomics for predictive assessment of brain parcellations. *NeuroImage* **2021**, *238*, 118170. [[CrossRef](#)]

**Disclaimer/Publisher’s Note:** The statements, opinions and data contained in all publications are solely those of the individual author(s) and contributor(s) and not of MDPI and/or the editor(s). MDPI and/or the editor(s) disclaim responsibility for any injury to people or property resulting from any ideas, methods, instructions or products referred to in the content.